THE JOURNAL OF PHYSICAL CHEMISTRY C
A JOURNAL OF THE AMERICAN CHEMICAL SOCIETY

pubs.acs.org/JPCC

Article

Modeling of Space-Charge Layers in Solid-State Electrolytes: A Kinetic Monte Carlo Approach and Its Validation

Leon Katzenmeier,[⊥] Manuel Gößwein,[⊥] Alessio Gagliardi,* and Aliaksandr S. Bandarenka*

Cite This: *J. Phys. Chem. C* 2022, 126, 10900−10909

Read Online

ACCESS | Metrics & More | Article Recommendations | Supporting Information

ABSTRACT: The space-charge layer (SCL) phenomenon in Li^+-ion-conducting solid-state electrolytes (SSEs) is gaining much interest in different fields of solid-state ionics. Not only do SCLs influence charge-transfer resistance in all-solid-state batteries but also are analogous to their electronic counterpart in semiconductors; they could be used for Li^+-ionic devices. However, the rather "elusive" nature of these layers, which occur on the nanometer scale and with only small changes in concentrations, makes them hard to fully characterize experimentally. Theoretical considerations based on either electrochemical or thermodynamic models are limited due to missing physical, chemical, and electrochemical parameters. In this work, we use kinetic Monte Carlo (kMC) simulations with a small set of input parameters to model the spatial extent of the SCLs. The predictive power of the kMC model is demonstrated by finding a critical range for each parameter in which the space-charge layer growth is significant and must be considered in electrochemical and ionic devices. The time evolution of the charge redistribution is investigated, showing that the SCLs form within 500 ms after applying a bias potential.

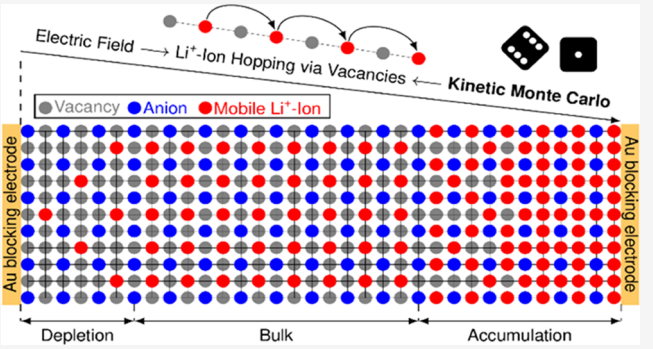

1. INTRODUCTION

Applications of ion-conducting solids range across energy storage,[1] energy conversion,[2] and ionic devices.[3] One possible application of Li^+-ion-conducting solid-state electrolytes (SSEs) is an all-solid-state battery, potentially enabling Li-metal anodes with the SSE posing as an impenetrable barrier to lithium dendrites.[4] While the ionic conductivity of the SSE is reaching the realm of their liquid counterparts,[5] the interface of the SSE toward materials with different electrochemical potentials, such as electrodes, remains a source for high ionic resistances.[6] Despite plenty of research into interface reactions,[7] formation of passivation layers,[8] and electrochemical stability,[9] the mere charge redistribution to accommodate the electrochemical potential difference between the two materials still lacks fundamental understanding. The so-called space-charge layer (SCL) in SSEs describes the phenomenon of charge accumulation or depletion at the interface of the SSE. As the only mobile species in the SSE are the cations, whether it is oxygen, lithium, or other ion-conducting solid, the formation of SCL is a mere redistribution of cations.

For Li^+-ion-conducting SSE, a variety of theoretical and experimental approaches have been used to investigate these evasive layers of altered Li^+-ion concentration within the SSE crystal lattice. As the electrochemical potential difference is the driving force for SCL occurrence, the effect can be investigated under blocking conditions by varying the potential drop across the interface. One study, based on a thermodynamic model with a numerical solution,[10] concludes that for a set of approximate parameters, the SCL extents tens, if not hundreds, of nanometers into the SSE at relatively low potentials. Based on electrochemical models, other theoretical considerations conclude that the impact should be negligible and the width of such a layer not larger than a few nanometers.[11]

In previous studies, we explored the formation of SCL under blocking conditions experimentally using electrochemical impedance spectroscopy (EIS)[12] and spectroscopic ellipsometry[13] on a model material system, a Li^+-ion-conducting glass-ceramic by Ohara Inc. The SCL width was found to range up to 200 nm into the SSE at a bias potential of 1.5 V with spectroscopic ellipsometry, which is in reasonable agreement with the capacitance of such a layer measured with impedance spectroscopy. The relatively wide layer was found to be in coexistence with a single Li^+-ion layer, which can be understood as the formation of a compact Helmholtz layer in liquid electrolytes (LEs).[14] The comparison of experimentally obtained widths and concentration changes to theoretical models is hindered by the uncertainties of physical parameters

Received: April 11, 2022
Revised: June 12, 2022
Published: June 23, 2022

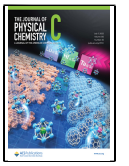

https://doi.org/10.1021/acs.jpcc.2c02481
J. Phys. Chem. C 2022, 126, 10900−10909

needed to calculate the impact of applied potential on the formation of an SCL.

The transport of ions in SSEs can be described by a thermally activated hopping mechanism between unoccupied lattice vacancies.[15,16] Unless a hopping transition is executed, each ion is spatially assigned to a vacancy. Such a configuration can be interpreted as a kind of localized state. Accordingly, the overall transport dynamics can be described by hops from one localized state to another. In this sense, ionic motion in SSEs fulfills the criteria of a so-called infrequent-event system. A very well-established theoretical approach to model such systems is the kinetic Monte Carlo (kMC) method. In general, kMC methods are a special subclass of Monte Carlo algorithms that can simulate the time evolution of nondeterministic systems. kMC models have been developed for numerous different applications such as charge transport in disordered organic semiconductors,[17−20] crystal growth,[21,22] chemical reaction networks,[23−26] vacancy diffusion,[27,28] and electrochemical systems.[29−32] In the direct context of solid-state electrolytes, kMC also has been applied. For instance, Wolverton and co-workers calculated the room-temperature ion conductivities of cation- and anion-substituted $LiBH_4$-based SSEs.[33] Very recently, Dean et al. showed that grain boundary space-charge regions in SSEs can exhibit over- as well as underscreening.[34] However, there is no kMC model that captures the experimentally observed SCL growth into the SSE, perpendicular to the electrode, for either fully depleted or fully occupied vacancy lattice.

In this work, we present a predictive kinetic Monte Carlo model for the SCL formation in SSEs, which features a perpendicular growth regime. The model requires only a minimal set of input parameters to simulate the spatial extent of the SCLs formed for various parameters and bias potentials. We use a standard parameter set based on previous investigations to validate the model and compare the results to experiments. Furthermore, a sensitivity analysis reveals the impact of physical parameters and material properties, which can assess the relevance of SCL for a given, new material system. As kinetic Monte Carlo simulations inherently allow calculations of the time evolution of concentration profiles, the dynamics of SCL formation are investigated.

2. THEORY AND MODEL

As outlined above, SSEs transfer ions through a hopping mechanism in a crystal lattice, which typically consists of immobile anions as a backbone and a sublattice of vacancies in which the ions move. As the SCL phenomenon in blocking conditions is a mere redistribution of mobile charges, it is essential to notice the physical boundaries. For clarity, only mobile cations are considered, even though theory[35] suggests that not all cations are mobile at room temperature. The mobile and immobile cations are located within the anion lattice, where anions simply neutralize their respective immobile cations. However, the mobile cations are the drivers of ionic conductivity and, therefore, can accumulate or deplete in a certain region. Anion mobility plays a crucial role in polymer-based SSEs,[36] which is neglected in this work. On the one hand, the anion mobility must be low in full ASSB cells to promote interfacial stability.[37] On the other hand, the movement of anions would certainly play a role in the lattice constants and crystal structure, an effect that could be part of future kMC simulations.

The concentration of cations is given by c_{Li^+}, and it is important to differentiate between three scenarios.

(i) An electroneutral lattice, where c_{Li^+} and the anion concentration compensate. This is the case in the bulk of the SSE and will be described as $c_{Li^+,bulk}$.

(ii) A fully depleted lattice, where no mobile Li^+ ions are left. This forms a maximally electronegative lattice, and the Li^+-ion concentration is c_{min}.

(iii) A full lattice, where no free vacancies are left. This forms a maximally electropositive lattice, and the Li^+-ion concentration is c_{max}.

The cation concentration is therefore limited to $c_{min} \leq c_{Li^+} \leq c_{max}$ and reaches a nonzero equilibrium of $c_{Li^+,bulk}$ in the bulk SSE. While the polarization state of the SSE does not influence the concentration limits, the material (crystal lattice) and the temperature will significantly impact the concentrations.

When the SSE is brought into contact with a material of different electrochemical potentials (either inherent or by applying a bias potential), the potential drops within a certain region, which is not electroneutral. The SCL, therefore, occurs in the vicinity of the interface. The concept of SCL formation is like that of electrical double layers (EDLs) at the liquid electrolyte (LE)/electrode interface.[38] In EDLs, the anions and cations accumulate to form charged layers with relatively small thicknesses.[39] The amount of charge and spatial distribution of the EDL causes the electrical potential to drop within this short-range and, therefore, the bulk of the LE to stay electroneutral. While the Li^+ concentration is only limited by the volume in LEs, and thus LEs allow a significantly higher charge density in SSEs, the limits of Li^+ concentration are given by $c_{min} \leq c_{Li^+} \leq c_{max}$. The limits in charge density are responsible for the formation of thicker layers when the same amount of charge must be held to screen the electrochemical potential difference.

The kinetic Monte Carlo method is a stochastic algorithm to simulate the sequential time evolution of a system through different states within its configuration space. As a fundamental concept, kMC relies on coarse-graining system dynamics. The investigated system is reduced to a set of long-term states $\{i\}$ connected by discrete transitions. In each state i, the system may evolve to a set of possible states $\{j\}$. Every transition is governed by a transition rate, k_{ij}, which captures the actual physical process inducing the transition $i \rightarrow j$. The transition rates are crucial input parameters for the kMC model. Typically, they are either based on underlying physical models or taken from experiments. The relative probability of a certain state-to-state transition is directly proportional to the magnitude of the corresponding rate

$$P_{ij} = \frac{k_{ij}}{k_{tot}} = \frac{k_{ij}}{\sum_j k_{ij}} \tag{1}$$

where k_{tot} denotes the total rate of all possible transitions. In the so-called Monte Carlo step, two uniformly distributed random numbers r_1, $r_2 \in (0,1)$ are drawn to determine (1) which transition, μ, is executed and (2) how much time, τ, has passed before the transition is performed. Via the first random number r_1, we select transition μ from the set of all transition probabilities $\{P_{ij}\}$ according to the inequation

$$\sum_{j=1}^{\mu-1} P_{ij} < r_1 \leq \sum_{j=1}^{\mu} P_{ij} \tag{2}$$

The second random number r_2 yields the corresponding time-step

https://doi.org/10.1021/acs.jpcc.2c02481
J. Phys. Chem. C 2022, 126, 10900−10909

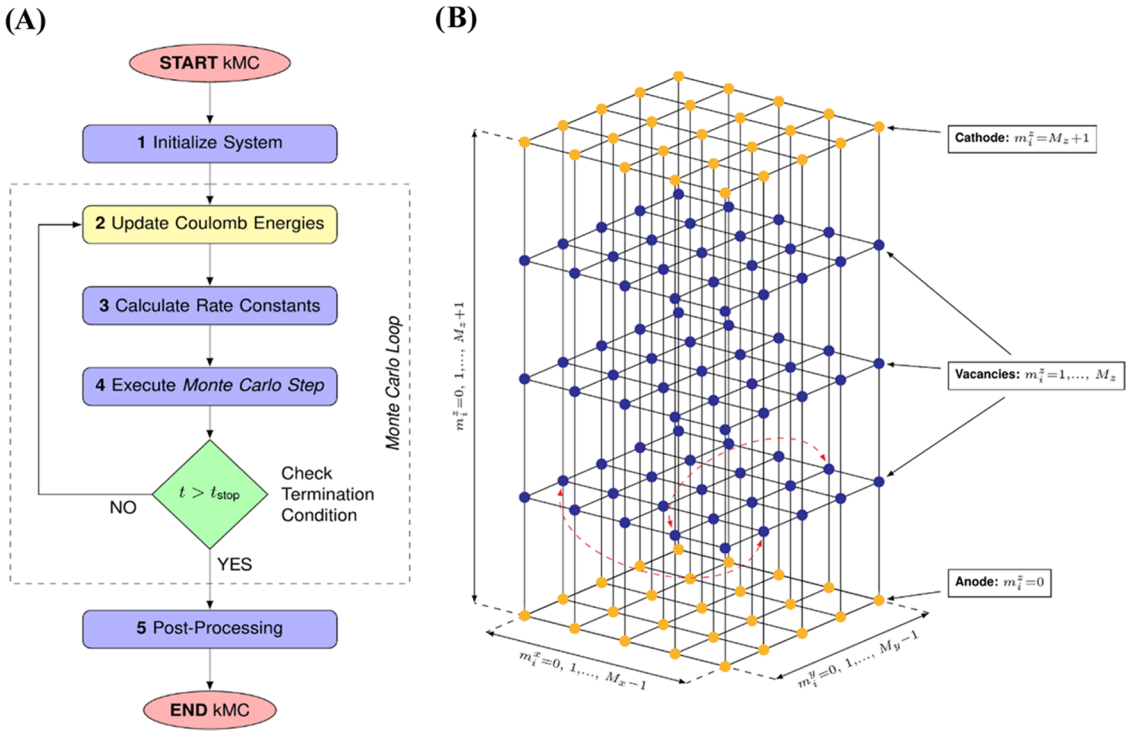

Figure 1. Kinetic Monte Carlo Method. (A) System specialized flowchart of the kMC algorithm for simulating the SCL formation in SSEs. (B) Representation of the experimental set-up as a grid of discrete sites. Blue and yellow sites correspond to vacancies and contact nodes, respectively. The dashed red arrows visualize the periodic boundary conditions applied in the *xy*-plane. From a geometrical point of view, each site i is described by an index triplet (m_i^x, m_i^y, m_i^z), and the total number of sites in *xyz*-directions are given by M_x, M_y, and M_z, respectively.

$$\tau = -\frac{\ln(r_2)}{k_{tot}} \tag{3}$$

Equations 2 and 3 are related to the so-called *n*-fold or direct method outlined in ref 40. Subsequently, the system state is updated according to the chosen transition, μ, and the simulated time, t, is advanced by τ. In the new system state, the transition rates must be recalculated before another Monte Carlo step can be performed. Repeated execution of this procedure results in the stochastic time evolution of the system. Usually, the simulation is completed after a user-defined termination condition, e.g., the simulated time exceeds a certain threshold, $t \geq t_{stop}$.

The general algorithm must be adapted accordingly to simulate the SCL formation in SSEs via kMC (see Figure 1A) for a simplified flowchart. In the current study, the application of the kMC algorithm boils down to five essential steps:

1. System initialization: The experimental set-up is mapped onto a set of discrete sites that store geometrical (e.g., position) as well as physical properties (e.g., potential energy). The sites either represent vacancies or contact nodes. At the beginning of the simulation, vacancies are randomly occupied by Li^+ ions according to input bulk density $c_{Li^+,bulk}$.
2. Update of Coulombic energies: The local hopping rates of each Li^+ ion depend on the mutual Coulombic interactions with all other cations and a neutralizing anionic background. Since the configuration of mobile Li^+ ions changes in each kMC step, the Coulombic energies must be updated according to the new configuration prior to the recalculation of hopping rates.
3. Calculation of rate constants: As outlined above, the SCL formation in SSEs corresponds to a mere redistribution of mobile Li^+ ions. To capture this process on a local scale, we compute the hopping rates for each Li^+ ion to all unoccupied nearest-neighbor vacancies. The magnitude of these rates is determined by the physical and geometrical properties of the investigated SSE sample as well as the local potential energy surface.
4. Execution of the Monte Carlo step: Two uniform random numbers $r_1, r_2 \in (0,1)$ are drawn. Based on eq 2, r_1 is used to select the ion hopping transition to be executed and, based on eq 3, r_2 is used to compute simulated time τ prior to the transport event. Afterward, we check whether simulated time t exceeds the steady-state time t_{stop}, which can be obtained by trial simulations. If $t < t_{stop}$, another simulation step is performed. The repetitive execution of steps 2−4 is also denoted the Monte Carlo loop.
5. Postprocessing: If the termination condition is fulfilled, the Monte Carlo loop is exited. As a final step, the raw output data of the simulation are converted into meaningful physical quantities. Here, we transform the local relative vacancy occupation times into a corresponding local Li^+-concentration profile, which enables the calculation of numerous other characteristic quantities such as the potential profile and the SCL thickness/capacitance.

3. MODELING AND SIMULATION SETUP

Next, we outline the detailed kMC model set-up of an SSE sample confined between two gold blocking electrodes, see Figure 1B. The sample is represented by a three-dimensional primitive orthorhombic lattice constituted of a total number of

https://doi.org/10.1021/acs.jpcc.2c02481
J. Phys. Chem. C 2022, 126, 10900−10909

$M_x \times M_y \times M_z$ sites. Each site i corresponds to a vacancy and is geometrically defined by an index triplet $\boldsymbol{m} = (m_i^x, m_i^y, m_i^z)$, which determines physical position $\boldsymbol{r} = \boldsymbol{m}\cdot\boldsymbol{a}$ via lattice constants $\boldsymbol{a} = (a_x,a_y,a_z)^T$. Accordingly, the total physical size of the lattice is given by $X \times Y \times Z = M_x a_x \times M_y a_y \times M_z a_z$. In the xy-plane, periodic boundary conditions are assumed; in the z-direction, the sample is stacked between two ideal gold contacts ($\varepsilon_r \to \infty$) at $z = 0$ and Z, respectively. The local potential energy per vacancy site, E_i, is the superposition of three contributions

$$E_i = E_i^{\mathrm{ref}} + E_i^{\mathrm{F}} + E_i^{\mathrm{C}} \tag{4}$$

where E_i^{ref} denotes the energy defined by a reference electrode, E_i^{F} is the contribution from an external electric field, and E_i^{C} is the potential generated by Coulombic interactions of mobile cations and their respective immobile anions. In the scope of this study, we arbitrarily set $E_i^{\mathrm{ref}} = 0$. E_i^{F} is modeled as a linear potential drop along the z-axis

$$E_i^{\mathrm{F}} = (q\phi_b - \Delta W)\frac{z_i}{Z} \tag{5}$$

where ϕ_b denotes the applied bias potential, ΔW is the difference in electrode work functions, and z_i is the z-coordinate of site i. Assuming two identical blocking electrodes, we may set $\Delta W = 0$. E_i^{C} is composed of the cation−cation interaction, E_i^{cc}, and the anion−cation interaction E_i^{ac}. Both components are treated accurately via a three-dimensional Ewald summation following the methodology established by Casalegno et al.[41,42] Since the anions are immobile, E_i^{ac} can be computed before the simulation. In contrast, E_i^{cc} is a function of the current position of all mobile cations and, thus, must be calculated and updated dynamically during the simulation. Note that our model does not consider immobile cations as they are locally neutralized by respective immobile anions from the underlying anion lattice. Accordingly, the local potential energy landscape defined by eq 4 is not altered by the presence of immobile cations and, thus, they do not modify the transport dynamics of the mobile cations.

The experimental set-up applies sample lengths, L_s, of about 150 μm—a length scale that cannot be covered by any standard particle-based kMC simulation. However, the previous experimental findings demonstrate that SCL formation is restricted to a rather small fraction of the actual sample length (about 0.25%). For the most part, the sample remains in bulk conditions. Hence, we can artificially decrease L_s without disturbing the actual SCL formation. The only requirement is that the depletion and accumulation layers must not overlap. For instance, assuming SCL widths in the range of 200−300 nm (as recently determined by spectroscopic ellipsometry),[13] it is sufficient to consider a sample length of 1 μm. The artificial reduction of the experimental sample length relies on the fundamental assumption that SCL formation is independent of the device length. This hypothesis stands in direct contrast to the results from the thermodynamic model developed by Braun et al.[10] Later, we will prove the validity of our hypothesis via a sensitivity analysis with respect to L_s. It is true that a shortened sample length does not perturb the steady-state distribution of Li^+ ions. However, the time evolution of the SCL formation is undoubtedly a function of L_s as the sample length determines the electric field strength, ε, and, thus, the drift velocity, v_d, of Li^+ ions. In the present study, we assume that ε is sufficiently low to guarantee a linear relationship between field strength and drift velocity.

The most critical aspect of the kMC model is the incorporation of a lower and an upper limit for the concentration of mobile Li^+ ions, in the following denoted c_{min} and c_{max}, respectively. The lower limit is naturally given by $c_{\mathrm{min}} = 0$. For the upper limit, we choose a rather pragmatic approach: the kMC model discretizes the SSE sample into a primitive orthorhombic lattice of vacancies that can only be occupied by one mobile Li^+ ion at a time. Accordingly, the maximum possible concentration is dictated by the inverse volume of a unit cell, $c_{\mathrm{max}} = a_x \times a_y \times a_z)^{-1}$. The required lattice parameters of the vacancy grid are then chosen based on the given input value for c_{max}. For instance, imposing $c_{\mathrm{max}} = 4.5 \times 10^{18}$ cm^{-3} yields lattice constants of $a_x = a_y = a_z \approx 6$ nm. The choice of c_{max} also affects the strength of local Coulombic interactions. Low values of c_{max} result in large lattice constants and, thus, amplified electrostatic screening. All lattice parameters applied in this study are summarized in Table S1, Supporting Information (SI).

The simulation starts at $t = 0$ with a random distribution of Li^+ ions. The number of mobile cations is imposed by the volume of the simulation box and the given input bulk concentration $c_{\mathrm{Li^+}}^{\mathrm{bulk}}$. To ensure electroneutrality, we assume a homogeneous anionic background. The hopping of cations between two vacancy sites i and j is captured via the Miller−Abrahams formula[43]

$$k_{ij} = k_0 \cdot \begin{cases} \exp\left(-\dfrac{\Delta E_{ij}}{k_B T}\right), & \Delta E_{ij} < 0 \\ 1, & \Delta E_{ij} \geq 0 \end{cases} \tag{6}$$

where k_0 is the attempt-to-hop frequency, ΔE_{ij} denotes the difference in potential energy between vacancies i and j, k_B is the Boltzmann constant, and T gives the absolute temperature. Hopping events are restricted to nearest-neighbor vacancies. The maximum attempt-to-hop frequency is estimated from the experimentally determined activation barrier for diffusion, E_a, according to an Arrhenius equation[44]

$$k_0 = \frac{k_B T}{h}\exp\left(-\frac{E_a}{k_B T}\right) \tag{7}$$

where h is the Planck constant. All simulations were conducted for $T = 300$ K and $E_a = 0.42$ eV resulting in a maximum hopping rate of $k_0 \approx 0.55 \times 10^6$ s^{-1}. For nearest-neighbor hopping, the root mean diffusion length is given by the chosen lattice constants. To incorporate the influence of different lattice constants in the xyz-direction, we scale k_0 by either a_x^{-2} or a_y^{-2} or a_z^{-2}, respectively, following the classical random walk model for diffusive motion.[45] For reasons of completeness, we note that the gold contacts are inert, corresponding to the experimental blocking conditions. In the scope of this study, the contacts exclusively represent electrostatic boundary conditions.

4. COMPUTATIONAL ASPECTS AND DATA EVALUATION

In general, the simulation of the SCL formation in SSEs via kMC is a computationally demanding task. The high computational effort arises from the high number of mobile Li^+ ions (N = 3000−6000 depending on the chosen set of input parameters) as the dynamic calculation of Coulombic energies via an optimized Ewald summation still scales as $O(N^{3/2})$.[46] To make the kMC simulations feasible in a reasonable amount of simulation time, we apply four different techniques to reduce the computational effort:

1. Application of modern C++: Our in-house kMC framework[18] is implemented within modern C++ and

https://doi.org/10.1021/acs.jpcc.2c02481
J. Phys. Chem. C 2022, 126, 10900−10909

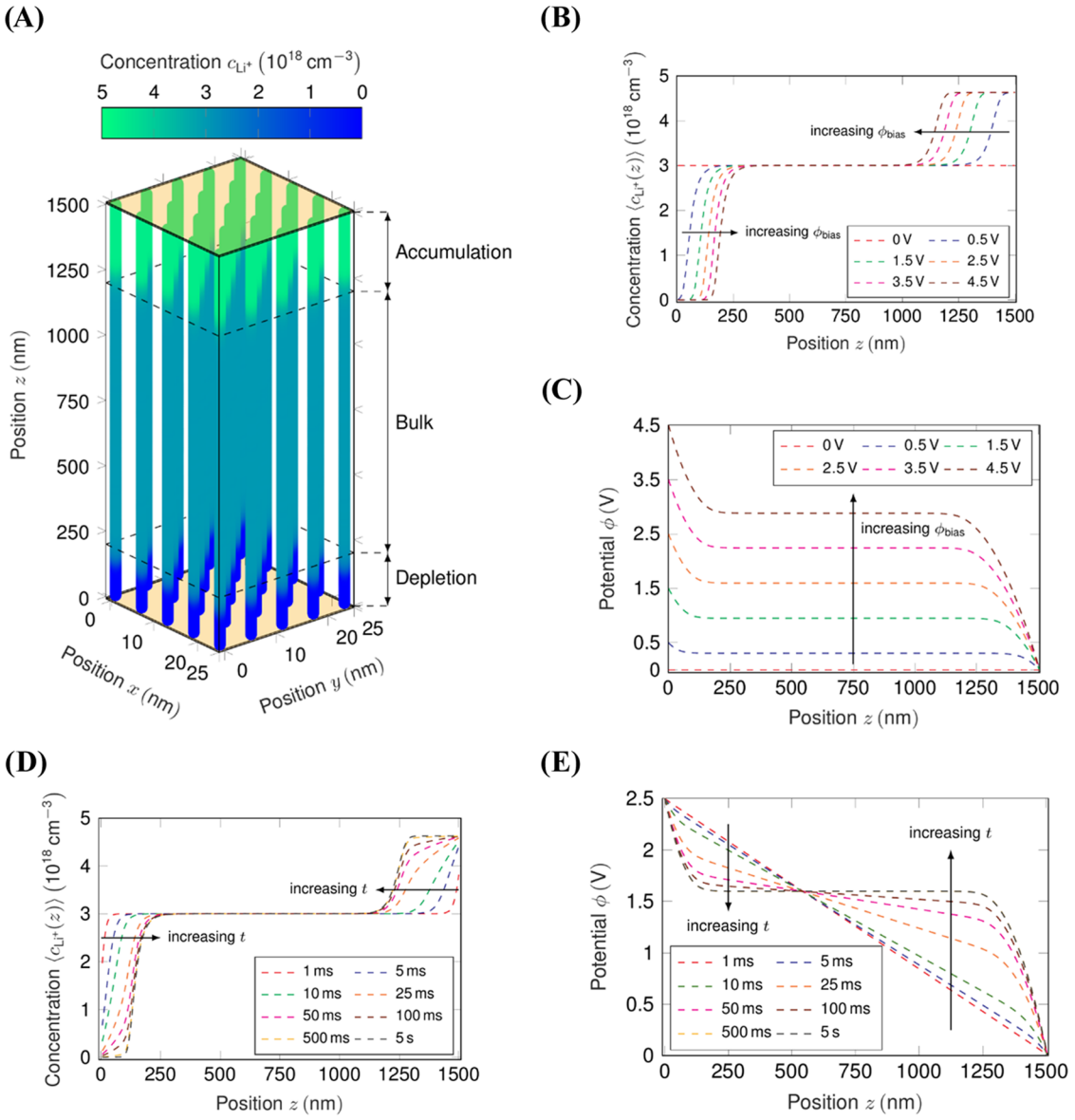

Figure 2. Simulation results for the standard parameter set. (A) Local concentration profile, $c_{Li^+}(x,y,z)$. (B) Averaged concentration profiles, $\langle c_{Li^+}(z)\rangle$, for variable ϕ_{bias} and (C) corresponding potential profiles calculated via eq 9. (D) Time evolution of $\langle c_{Li^+}(z)\rangle$ for $\phi_{bias} = 2.5\ V$ and (E) corresponding potential profiles. For the given sample length, the SCL formation reaches a steady state after approximately 500 ms.

makes heavy use of novel features from C++17 (e.g., parallel algorithms) and C++20 (e.g., ranges and views).

2. Caching of pair potentials: The system discretization is based on a regular grid that enables the precalculation (or caching) of all pair potentials possibly required by the Ewald summation. A detailed discussion can be found in ref 39.
3. Dipole-update method: By introducing a fictitious dipole into the update of Coulombic energies, the computational effort connected to nonmoving Li^+ ion can be reduced to $O(N)$. The methodology was originally introduced in ref 47.
4. Parallelization: The update of Coulombic energies and the calculation of rate constants (cf. steps 2 and 3 in Figure 1A) correspond to loops running over the total number of involved Li^+ ions. The computations for each Li^+ ion are independent of each other and, thus, can be trivially parallelized.

Based on these techniques, we obtain an average simulation time per fixed input parameter combination of approximately 4 days using eight cores (Intel Xeon E-2288G@3.70 GHz) on the HPC server cluster of the Chair of Nano and Quantum Sensors at the Technical University of Munich.

The actual output quantities of the kMC model are time-dependent, three-dimensional profiles of relative vacancy occupation times. However, if not stated otherwise, we will consider the steady-state configuration, which enables us to drop the time dependency. From the relative occupation times, local concentration profiles, $c_{Li^+}(x,y,z)$, can be computed (cf. ref 39). Due to the homogeneity of the three-dimensional concentration profiles in the xy-plane (see Figure 1A), we may calculate averaged concentration profiles, $\langle c_{Li^+}(z)\rangle$, to simplify visualization and further discussion of the simulation results. The averaged concentration profiles, in turn, can be used to compute the average charge density

$$\langle \rho(z)\rangle = q(\langle c_{Li^+}(z)\rangle - \langle c_{A^-}(z)\rangle) \tag{8}$$

https://doi.org/10.1021/acs.jpcc.2c02481
J. Phys. Chem. C 2022, 126, 10900−10909

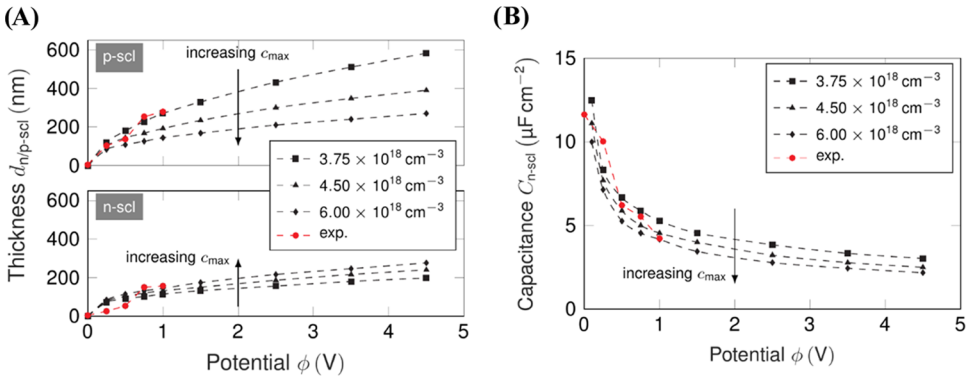

Figure 3. Comparison to experimental results. (A) SCL thicknesses $d_{n/p\text{-}scl}$ as a function of ϕ_{bias}. The thicknesses of depletion and accumulation layer from kMC were obtained via eqs 10 and 11, respectively. Red dots correspond to the experimental results obtained by spectroscopic ellipsometry. (B) Capacitance of the depletion layer, $C_{n\text{-}scl}$, as a function of ϕ_{bias}. Capacitances from kMC were calculated via eq 12. Red dots correspond to the experimental results obtained by electrochemical impedance spectroscopy. In both plots, black squares, triangles, and diamonds illustrate the kMC results for different values of c_{max}.

where q is the elementary charge and $\langle c_{A^-}(z)\rangle = c_{Li^+}^{bulk}$ = const. is the concentration of the homogeneously distributed anionic background. Based on the one-dimensional charge density profiles, the Poisson equation may be solved to obtain corresponding potential profiles $\phi(z)$

$$\frac{\partial^2}{\partial^2 z}\phi(z) = -\frac{\langle \rho(z)\rangle}{\varepsilon_0 \varepsilon_r} \tag{9}$$

where ε_0 is the vacuum permittivity and ε_r is the relative permittivity of the bulk SSE. To make the simulation results comparable to the experimental measurements, we have also determined the thicknesses of the accumulation and depletion layer, in the following denoted $d_{p\text{-}scl}$ and $d_{n\text{-}scl}$, respectively. For this purpose, we have defined simple criteria to extract the extension of the SCLs from the one-dimensional density profiles: The depletion layer is represented by the part of the concentration profile that fulfills the inequation

$$\langle c_{Li^+}(z)\rangle \leq (1-\delta)\cdot c_{Li^+}^{bulk} \tag{10}$$

where $\delta = 0.1$ is a threshold value chosen according to the resolution of the SCL thicknesses determined by spectroscopic ellipsometry. Analogously, the accumulation layer is defined by

$$\langle c_{Li^+}(z)\rangle \geq (1+\delta)\cdot c_{Li^+}^{bulk} \tag{11}$$

Finally, the SCL thicknesses are used to compute corresponding area-specific capacitances via the well-known formula of a parallel-plate capacitor

$$C_{n/p-scl} = \frac{\varepsilon_0 \varepsilon_r}{d_{n/p-scl}} \tag{12}$$

where ε_r denotes the relative permittivity of the bulk SSE.

5. RESULTS AND DISCUSSION

Within the scope of this study, we want to investigate the SCL formation in SSEs with different physical properties. For this purpose, we vary the bulk concentration $c_{Li^+}^{bulk} \in [5 \times 10^{17}, 3 \times 10^{18}, 1 \times 10^{19}]$ cm^{-3}, the maximum concentration for accumulation of Li^+ ions, $c_{max} \in [1.25, 1.5, 2.0]\cdot c_{Li^+}^{bulk}$, and relative permittivity of the bulk SSE, $\varepsilon_r \in [100, 677, 1400]$. Additionally, the external bias potential ϕ_{bias} is swept from 0 to 4.5 V in steps of 0.5 V to cover the full operating regime in a potential all-solid-state battery application. To elucidate the characteristic time scale of ion redistribution, we have also simulated the time evolution of the SCL formation for 5 s for a set of standard input parameters determined in previous studies:

- Bulk concentration: $c_{Li^+}^{bulk} = 3 \times 10^{18}$ cm^{-3}
- Maximum concentration: $c_{max} = 1.5\ c_{Li^+}^{bulk}$ (corresponds to the thickness ratio obtained by spectroscopic ellipsometry[13])
- Permittivity: $\varepsilon_r = 677$ (corresponds to the value determined by impedance spectroscopy[12])
- Bias potential: $\phi_{bias} = 2.5$ V

Since kMC is a stochastic algorithm, any statistically significant output quantity must be obtained as an average over a sufficient number of simulation runs. Here, we mostly consider steady-state quantities for which we may apply the block averaging technique as described in ref 39. In contrast, the results for the time-dependent SCL formation were generated by averaging over 50 independent simulation runs.

To rationalize the kMC simulation results, we first analyze the time-dependent ion redistribution for the standard input parameter set, see Figure 2. The local steady-state concentration profile, $c_{Li^+}(x,y,z)$, is illustrated in Figure 2A. The application of a positive bias potential leads to the formation of depletion and accumulation layers at the respective blocking electrodes, whereas the bulk SSE remains in an electroneutral condition. As outlined above, the homogeneity of the three-dimensional concentration profiles in the xy-plane allows us to consider averaged concentration profiles, $\langle c_{Li^+}(z)\rangle$, in the following. Figure 2B shows the averaged concentration profiles of the standard parametrization for variable ϕ_{bias}. As expected, the SCL formation only occurs for nonzero bias potentials, and the SCL grows perpendicularly into the SSE when the potential is increased. The Li^+ accumulation and depletion show an inherent asymmetry—due to the limits of accumulable and depletable charges: $c_{min} \leq c_{Li^+} \leq c_{max}$. If bulk concentration $c_{Li^+,bulk}$ is unevenly spaced between c_{min} and c_{max}, and the number of charges depleted and accumulated are equal, the SCLs will form asymmetrically.

The growth of the SCLs, however, does not scale linear—but rather reaches a plateau for high potentials. The density profile also shows that bulk stays indeed electroneutral as the Li^+ density is equal to the anion density. The bulk is therefore effectively screened from the influence of the bias potential, which can also be observed in Figure 2C, where the potential

https://doi.org/10.1021/acs.jpcc.2c02481
J. Phys. Chem. C 2022, 126, 10900−10909

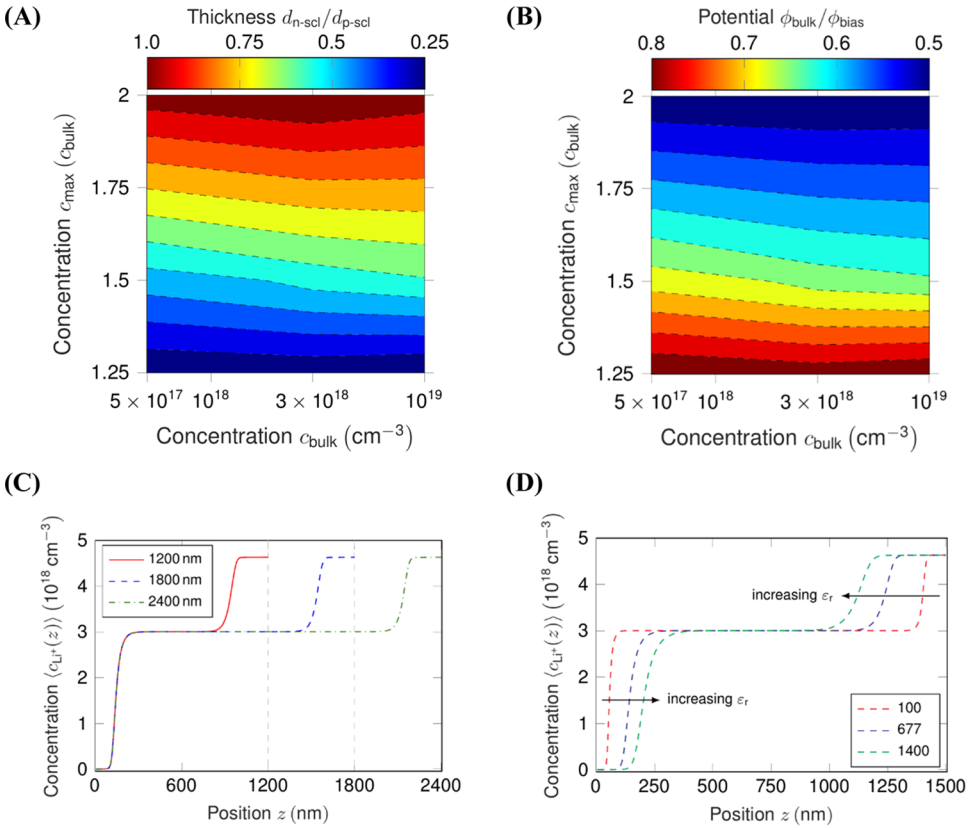

Figure 4. Sensitivity analysis. (A) Ratio $\frac{d_{n-scl}}{d_{p-scl}}$ as a function of c_{bulk} and c_{max} for $\varepsilon_r = 677$ and $\phi_{bias} = 2.5$ V. (B) Ratio $\frac{\phi_{bulk}}{\phi_{bias}}$ as a function of c_{bulk} and c_{max} for $\varepsilon_r = 677$ and $\phi_{bias} = 2.5$ V. (C) Averaged concentration profile, $\langle c_{Li^+}(z)\rangle$, of the standard parameter set for different sample lengths L_s. (D) Averaged concentration profile, $\langle c_{Li^+}(z)\rangle$, of the standard parameter set for different permittivities ε_r.

profiles are calculated via eq 9. From the potential profiles, the asymmetry in the potential drops can be observed, as in this case a higher potential drop occurs in the accumulation layer compared to the depletion layer. The bulk potential is, therefore, shifted upward to the applied potential if the depletion layer is thinner than the accumulation layer. To conclude this first part of our analysis, we discuss the time evolution of the averaged concentration and the potential for the standard parameter set, see Figure 2D,E, respectively. The redistribution of cations induces a distortion of the initially linear potential drop over the sample. The SCL formation essentially occurs on a time scale of roughly 500 ms for the given device length of 1500 nm. Afterward, accumulation and depletion of mobile Li^+ ions are negligible as recognizable by the identical potential profiles for 500 ms and 5 s. Assuming a linear relationship between electric field strength and drift velocity, we can scale up the time scale from kMC to an experimentally applied length of 150 μm, which results in an SCL formation time of 50 s.

With the physical validity of the model proven, the results can be compared to the experimental results from our previous studies.[12,13] Note that the experimental range of bias potentials is restricted to 0 V $\leq \phi_{bias} \leq$ 1 V to ensure that gold acts as a blocking electrode, see refs 12 and 48 for a detailed discussion. In contrast, the kMC simulations can be extended to larger potentials to extrapolate the trend in the experimental data. With the thickness of the SCLs being the most prominent parameter, the experimental results obtained by in situ spectroscopic ellipsometry are shown in Figure 3A with the typical asymmetric increase of thickness depending on whether the accumulation layer (positive biases) or the depletion layer (negative biases) are observed. The accumulation layer is roughly 1.5 times larger than the depletion layer. A plateau formation can be observed for potentials larger than 0.5 V, correlating to a fully depleted or filled lattice after which the SCL grows perpendicular to the SSE. Quantitatively, the thicknesses range from 50 to 330 nm depending on the applied bias. The kMC simulations agree to all observations if the physical parameters (Li^+-ion and vacancy concentration and dielectric constant) are chosen carefully. While the simulated bias potential range is larger than the experimentally feasible range, the same strong increase in SCL thickness can be observed when the bias potential is increased. The bias potential at which the SCL thickness is observed to be minimal in the experimental data matches that of 0 V bias potential in the kMC simulation, indicating that the electrochemical potential difference between the Au electrode and SSE is negligible. The experimentally determined spatial extent of the SCLs matches that of the kMC simulation for the standard parameters chosen—proving the closeness of the parameters to the true physical values.

There is a second property of the SCLs that can be validated experimentally, which is independent of the spatial extent: the capacitance. Experimentally, only the capacitance of the depletion layer is accessible, which is explained in previous work, see ref 12. The derivation of the SCL capacitance from the kMC simulations can be done by eq 12. Electrochemical impedance spectroscopy (EIS) was used to obtain the data in Figure 3B showing a strong decrease with increasing potential. The experimentally observed capacitances range between 4 and

https://doi.org/10.1021/acs.jpcc.2c02481
J. Phys. Chem. C 2022, 126, 10900−10909

12 $\mu F/cm^2$, which is in good quantitative agreement with the simulated capacitances. However, one exception is given by the capacitance value for 0 V bias potential. Here, we obtain a depletion layer thickness of 0 nm based on the criterion defined in eq 10, which would result in an infinitely large capacitance. This limitation is going to be addressed in future work by refining the simulation model as well as the criterion for extracting the SCL thicknesses. Nevertheless, the kMC simulations are capable of capturing the physical behavior of the experimentally predicted SCL formation for a wide range of bias potentials. Next, the sensitivity of the SCL formation on the input parameters is studied to see how material properties impact the thickness and asymmetry of SCLs.

As introduced above, three physical parameters are of fundamental importance to the kMC simulations: the Li^+-ion concentrations (bulk and maximal) and the dielectric constant. The impact of the limits on the Li^+-ion concentration can be split into two considerations: If the bulk Li^+-ion concentration varies, the accumulation layer should be unaffected as the upper Li^+ concentration is not dependent on the number of Li^+ ions present in the bulk. Therefore, only the depletion layer changes when the bulk Li^+-ion concentration is changed. For lower concentration deviations for a depleted lattice (i.e., lower bulk Li^+-ion concentration), the depletion layer must grow larger to hold a similar charge (assuming an equal potential drop and dielectric constant) and vice versa. However, the maximal concentration for Li^+ ion only impacts the accumulation layer formation by defining the maximal concentration change. The asymmetry is most easily observed when viewing the ratio of the accumulation layer to depletion layer thickness for a given potential. Figure 4A shows the dependence of the ratio $\frac{d_{n-scl}}{d_{p-scl}}$ for bulk densities between 5×10^{17} and 1×10^{19} cm^{-3} and maximal densities between 1.25 and 2 times the bulk density. The depletion and accumulation layer are of the same thickness if the accumulable concentration is the same as the depletable (i.e., $n_{max} = 2 \cdot n_{bulk}$), which is the same as claiming that the amount of concentration deviation is equal in both directions. If the accumulable concentration is much lower than the bulk concentration ($n_{max} = 1.25 \cdot n_{bulk}$), the accumulation layer grows much larger than the depletion layer as it cannot hold an equal amount of charge per volume. While these conclusions are to be expected from a concentration point of view and could have been predicted by merely claiming the charge distribution to happen within the boundaries and a certain number of charges moved from depletion to accumulation layer, the dependence of the ratio on the actual bulk Li^+-ion density is somewhat unexpected. A close look at the actual model input compared to the nominal value of c_{max}, see Table S1 (SI), explains this behavior. As shown in Figure 4A, the distribution of the ratio becomes more pronounced for higher bulk concentrations, a fact pointing toward a fundamental difference to the results from the aforementioned thermodynamic model.[10] Not only does this impact the thickness of the layers but also the potential of the bulk SSE—which is electroneutral and therefore has a constant potential, as shown in Figure 4B. The constant bulk potential is not right in the center between the two electrodes, i.e., $\phi_{bulk} = 0.5\ \phi_{bias}$, but shifted upward if the layers of not of equal widths.

While the asymmetry is affected by the charge carrier concentrations, as one would expect from basic electrochemical considerations, the impact of the sample or device length on the charge accumulation is not obvious. As shown in Figure 4C, the bulk SSE stays completely electroneutral—and should therefore not impact the charge accumulation. However, the Debye-like length, which has been described in the thermodynamic model, predicts a direct, inverse proportionality of the SCL thicknesses to the sample length. For a set of three different device lengths with otherwise equal parameters, the thicknesses of the SCLs are shown to be constant in Figure 4C. With a variation of the device length between 1.2 and 2.4 μm, the depletion layer does not change its position or shape, and the accumulation layer is simply shifted toward the geometric end of the device where it is in contact with the electrode. Therefore, the simulated charge carrier concentrations, and thus potential profiles, are independent of the device length. The impact of the dielectric constant, which ranges quite drastically between easily polarizable polymer electrolytes[49] and rigid SSEs,[50] is shown in Figure 4D. Higher polarizability leads to thicker SCLs, which agrees with the parallel plate capacitor analog as well as the Debye screening theory.

6. CONCLUSIONS

Overall, the findings of the kMC simulations are in good agreement with the thermodynamic simulations in ref 10, which predict the same perpendicular growth when the bias potential is increased. Not only do simulations show the same qualitative SCL growth but only employing two fundamental input parameters (the bulk and maximal charge carrier concentrations) can predict the order of magnitude of the SCL thicknesses in different materials. Physically coherent, the device/sample length is shown not to impact the SCL formation for three different lengths with only the electroneutral bulk growing. The calculated capacitances of the depletion layers match the experimental data of a previous study with—considering that only approximations of the input parameters are available—astonishing accuracy.

Moreover, a comparison of the accumulation layer, where the maximal ion concentration comes into play, cannot be achieved with impedance data, as this analysis is limited to the resistive depletion layer. The comparison of spectroscopic ellipsometry data of a previous study proves that the ratio of positive and negative SCLs is accurately represented by the kMC simulations.

Notably, the charge distributions can be directly transformed into potential profiles, which reveal that the potential drops are not equal at the two interfaces. The electrochemical stability of SSEs toward anode and cathode materials is a commonly discussed problem. When the stability of the anode and cathode is known, the charge carrier concentrations, therefore, allow to tune the bulk potential and thus the potential drops—possibly allowing higher overall voltages or different electrode materials.

■ ASSOCIATED CONTENT

Supporting Information

The Supporting Information is available free of charge at https://pubs.acs.org/doi/10.1021/acs.jpcc.2c02481.

Nominal and actual maximum concentrations in table format (PDF)

■ AUTHOR INFORMATION

Corresponding Authors

Alessio Gagliardi − *Department of Electrical and Computer Engineering, Technical University of Munich, 85748 Garching bei München, Germany;* orcid.org/0000-0002-3322-2190; Email: alessio.gagliardi@tum.de

https://doi.org/10.1021/acs.jpcc.2c02481
J. Phys. Chem. C 2022, 126, 10900−10909

Aliaksandr S. Bandarenka − *Physics of Energy Conversion and Storage, Physik-Department, Technische Universität München, 85748 Garching bei München, Germany; Catalysis Research Center TUM, 85748 Garching bei München, Germany;* orcid.org/0000-0002-5970-4315; Email: bandarenka@ph.tum.de

Authors

Leon Katzenmeier − *Physics of Energy Conversion and Storage, Physik-Department, Technische Universität München, 85748 Garching bei München, Germany; TUMint·Energy Research, 85748 Garching bei München, Germany*

Manuel Gößwein − *Department of Electrical and Computer Engineering, Technical University of Munich, 85748 Garching bei München, Germany;* orcid.org/0000-0002-4804-7954

Complete contact information is available at: https://pubs.acs.org/10.1021/acs.jpcc.2c02481

Author Contributions

⊥L.K. and M.G. contributed equally to this work.

Notes

The authors declare no competing financial interest.

■ ACKNOWLEDGMENTS

This work is part of the ASSB Bayern project funded by the Bavarian Ministry of Economic Affairs, Regional Development, and Energy. Furthermore, the authors acknowledge the European Union's Horizon 2020 FETOPEN 2018−2020 program "LION-HEARTED" under grant agreement no. 828984 for funding. A.S.B. and A.G. acknowledge financial support from TUM Innovation Network for Artificial Intelligence powered Multifunctional Material Design (ARTEMIS) and funding in the framework of Deutsche Forschungsgemeinschaft (DFG, German Research Foundation) under Germany's Excellence Strategy—EXC 2089/1—390776260 (e-conversion).

■ REFERENCES

(1) Goodenough, J. B. Energy Storage Materials: A Perspective. *Energy Storage Mater.* **2015**, *1*, 158−161.

(2) Isenberg, A. O. Energy Conversion Via Solid Oxide Electrolyte Electrochemical Cells at High Temperatures. *Solid State Ionics* **1981**, *3*−*4*, 431−437.

(3) Banno, N.; Sakamoto, T.; Iguchi, N.; Sunamura, H.; Terabe, K.; Hasegawa, T.; Aono, M. Diffusivity of Cu Ions in Solid Electrolyte and Its Effect on the Performance of Nanometer-scale Switch. *IEEE Trans. Electron Devices* **2008**, *55*, 3283−3287.

(4) Wang, C.; Bai, G.; Yang, Y.; Liu, X.; Shao, H. Dendrite-free All-solid-state Lithium Batteries with Lithium Phosphorous Oxynitride-modified Lithium Metal Anode and Composite Solid Electrolytes. *Nano Res.* **2019**, *12*, 217−223.

(5) Mertens, A.; Yu, S.; Schön, N.; Gunduz, D. C.; Tempel, H.; Schierholz, R.; Eichel, R. A.; et al. Superionic Bulk Conductivity in $Li_{1.3}Al_{0.3}Ti_{1.7}(PO_4)_3$ Solid Electrolyte. *Solid State Ionics* **2017**, *309*, 180−186.

(6) Yu, C.; Ganapathy, S.; Van Eck, E. R.; Wang, H.; Basak, S.; Li, Z.; Wagemaker, M. Accessing the Bottleneck in All-solid State Batteries, Lithium-ion Transport Over the Solid-electrolyte-electrode Interface. *Nat. Commun.* **2017**, *8*, No. 1086.

(7) Culver, S. P.; Koerver, R.; Krauskopf, T.; Zeier, W. G. Designing Ionic Conductors: The Interplay between Structural Phenomena and Interfaces in Thiophosphate-based Solid-state Batteries. *Chem. Mater.* **2018**, *30*, 4179−4192.

(8) Zhu, Y.; He, X.; Mo, Y. Origin of Outstanding Stability in the Lithium Solid Electrolyte Materials: Insights from Thermodynamic Analyses Based on First-principles Calculations. *ACS Appl. Mater. Interfaces* **2015**, *7*, 23685−23693.

(9) Ma, C.; Cheng, Y.; Yin, K.; Luo, J.; Sharafi, A.; Sakamoto, J.; Chi, M.; et al. Interfacial Stability of Li Metal–solid Electrolyte Elucidated Via in Situ Electron Microscopy. *Nano Lett.* **2016**, *16*, 7030−7036.

(10) Braun, S.; Yada, C.; Latz, A. Thermodynamically Consistent Model for Space-charge-layer Formation in a Solid Electrolyte. *J. Phys. Chem.C* **2015**, *119*, 22281−22288.

(11) de Klerk, N. J. J.; Wagemaker, M. Space-charge Layers in All-solid-state Batteries; Important or Negligible? *ACS Appl. Energy Mater.* **2018**, *1*, 5609−5618.

(12) Katzenmeier, L.; Helmer, S.; Braxmeier, S.; Knobbe, E.; Bandarenka, A. S. Properties of the Space Charge Layers Formed in Li-ion Conducting Glass Ceramics. *ACS Appl. Mater. Interfaces* **2021**, *13*, 5853−5860.

(13) Katzenmeier, L.; Carstensen, L.; Schaper, S. J.; Müller-Buschbaum, P.; Bandarenka, A. S. Characterization and Quantification of Depletion and Accumulation Layers in Solid-state Li^+-conducting Electrolytes Using in Situ Spectroscopic Ellipsometry. *Adv. Mater.* **2021**, *33*, No. 2100585.

(14) Watzele, S. A.; Katzenmeier, L.; Sabawa, J. P.; Garlyyev, B.; Bandarenka, A. S. Temperature Dependences of the Double Layer Capacitance of Some Solid/liquid and Solid/solid Electrified Interfaces. An Experimental Study. *Electrochim. Acta* **2021**, *391*, No. 138969.

(15) Park, M.; Zhang, X.; Chung, M.; Less, G. B.; Sastry, A. M. A Review of Conduction Phenomena in Li-ion Batteries. *J. Power Sources* **2010**, *195*, 7904−7929.

(16) Funke, K. Debye-Hückel-type Relaxation Processes in Solid Ionic Conductors: The Model. *Solid State Ionics* **1986**, *18*−*19*, 183−190.

(17) Bässler, H. Charge Transport in Disordered Organic Photoconductors. A Monte Carlo Simulation Study. *Phys. Status Solidi B* **1993**, *175*, 15−56.

(18) Kaiser, W.; Popp, J.; Rinderle, M.; Albes, T.; Gagliardi, A. Generalized Kinetic Monte Carlo Framework for Organic Electronics. *Algorithms* **2018**, *11*, No. 37.

(19) Kaiser, W.; Albes, T.; Gagliardi, A. Charge Carrier Mobility of Disordered Organic Semiconductors with Correlated Energetic and Spatial Disorder. *Phys. Chem. Chem. Phys.* **2018**, *20*, 8897−8908.

(20) Kaiser, W.; Gößwein, M.; Gagliardi, A. Acceleration Scheme for Particle Transport in Kinetic Monte Carlo Methods. *Chem. Phys.* **2020**, *152*, No. 174106.

(21) Piana, S.; Gale, J. D. Three-dimensional Kinetic Monte Carlo Simulation of Crystal Growth from Solution. *J. Cryst. Growth* **2006**, *294*, 46−52.

(22) Rak, M.; Izdebski, M.; Brozi, A. Kinetic Monte Carlo Study of Crystal Growth from Solution. *Comput. Phys. Commun.* **2001**, *138*, 250−263.

(23) Dybeck, E. C.; Plaisance, C. P.; Neurock, M. Generalized Temporal Acceleration Scheme for Kinetic Monte Carlo Simulations of Surface Catalytic Processes by Scaling the Rates of Fast Reactions. *J. Chem. Theory. Comput.* **2017**, *13*, 1525−1538.

(24) Jørgensen, M.; Gronbeck, H. Scaling Relations and Kinetic Monte Carlo Simulations to Bridge the Materials Gap in Heterogeneous Catalysis. *ACS Catal.* **2017**, *7*, 5054−5061.

(25) Jørgensen, M.; Grönbeck, H. MonteCoffee: A Programmable Kinetic Monte Carlo Framework. *J. Chem. Phys.* **2018**, *149*, No. 114101.

(26) Jørgensen, M.; Grönbeck, H. Selective Acetylene Hydrogenation Over Single-atom Alloy Nanoparticles by Kinetic Monte Carlo. *J. Am. Chem. Soc.* **2019**, *141*, 8541−8549.

(27) Magna, A.; Coffa, S.; Colombo, L. A Lattice Kinetic Monte Carlo Code for the Description of Vacancy Diffusion and Self-organization in Si. *Nucl. Instrum. Methods Phys. Res., Sect. B* **1999**, *148*, 262−267.

(28) Grabowski, M.; Rogal, J.; Drautz, R. Kinetic Monte Carlo Simulations of Vacancy Diffusion in Nondilute Ni-X (X = Re, W, Ta) Alloys. *Phys. Rev. Mater.* **2018**, *2*, No. 123403.

(29) Drews, T. O.; Radisic, A.; Erlebacher, J.; Braatz, R. D.; Searson, P. C.; Alkire, R. C. Stochastic Simulation of the Early Stages of Kinetically Limited Electrodeposition. *J. Electrochem. Soc.* **2006**, *153*, C434.

(30) Andreaus, B.; Eikerling, M. Active Site Model for Co Adlayer Electrooxidation on Nanoparticle Catalysts. *J. Electroanal. Chem.* **2007**, *607*, 121−132.
(31) Pornprasertsuk, R.; Cheng, J.; Huang, H.; Prinz, F. B. Electrochemical Impedance Analysis of Solid Oxide Fuel Cell Electrolyte Using Kinetic Monte Carlo Technique. *Solid State Ionics* **2007**, *178*, 195−205.
(32) Blanquer, G.; Yin, Y.; Quiroga, M. A.; Franco, A. A. Modeling Investigation of the Local Electrochemistry in Lithium-O_2 Batteries: A Kinetic Monte Carlo Approach. *J. Electrochem. Soc.* **2016**, *163*, A329.
(33) Yao, Z.; Kim, S.; Michel, K.; Zhang, Y.; Aykol, M.; Wolverton, C. Stability and Conductivity of Cation-and Anion-substituted LiBH 4-based Solid-state Electrolytes. *Phys. Rev. Mater.* **2018**, *2*, No. 065402.
(34) Dean, J. M.; Coles, S. W.; Saunders, W. R.; McCluskey, A. R.; Wolf, M. J.; Walker, A. B.; Morgan, B. J. Overscreening and Underscreening in Solid-electrolyte Grain Boundary Space-charge Layers. *Phys. Rev. Lett.* **2021**, *127*, No. 135502.
(35) Martin, S. W.; Yao, W.; Berg, K. Space Charge Polarization Measurements As a Method to Determine the Temperature Dependence of the Number Density of Mobile Cations in Ion Conducting Glasses. *Z. Phys. Chem.* **2009**, *223*, 1379−1393.
(36) Armand, M. Polymer Solid Electrolytes - an Overview. *Solid State Ionics* **1983**, *9*−*10*, 745−754.
(37) Zhang, H.; Chen, F.; Lakuntza, O.; Oteo, U.; Qiao, L.; Martinez-Ibañez, M.; Armand, M.; et al. Suppressed Mobility of Negative Charges in Polymer Electrolytes with an Ether-functionalized Anion. *Angew. Chem.* **2019**, *131*, 12198−12203.
(38) Aizawa, Y.; Yamamoto, K.; Sato, T.; Murata, H.; Yoshida, R.; Fisher, C. A.; Hirayama, T.; et al. In situ electron holography of electric potentials inside a solid-state electrolyte: effect of electric-field leakage. *Ultramicroscopy* **2017**, *178*, 20−26.
(39) Bohinc, K.; Kralj-Iglič, V.; Iglič, A. Thickness of Electrical Double Layer. Effect of Ion Size. *Electrochim. Acta* **2001**, *46*, 3033−3040.
(40) Gillespie, D. T. Exact Stochastic Simulation of Coupled Chemical Reactions. *J. Phys. Chem. A* **1977**, *81*, 2340−2361.
(41) Casalegno, M.; Raos, G.; Po, R. Methodological Assessment of Kinetic Monte Carlo Simulations of Organic Photovoltaic Devices: The Treatment of Electrostatic Interactions. *J. Phys. Chem. C* **2010**, *132*, No. 094705.
(42) Casalegno, M.; Bernardi, A.; Raos, G. Numerical Simulation of Photocurrent Generation in Bilayer Organic Solar Cells: Comparison of Master Equation and Kinetic Monte Carlo Approaches. *J. Phys. Chem. B* **2013**, *139*, No. 024706.
(43) Miller, A.; Abrahams, E. Impurity Conduction at Low Concentrations. *Phys. Rev.* **1960**, *120*, 745.
(44) Atkins, P.; De Paula, J.; Keeler, J. *Atkins' Physical Chemistry*; Oxford University Press: New York, 2018.
(45) Chandrasekhar, S. Stochastic Problems in Physics and Astronomy. *Rev. Mod. Phys.* **1943**, *15*, 1.
(46) Allen, M. P.; Tildesley, D. J. *Computer Simulation of Liquids*; Oxford University Press: New York, 2017.
(47) van der Kaap, N. J.; Koster, L. J. A. Massively Parallel Kinetic Monte Carlo Simulations of Charge Carrier Transport in Organic Semiconductors. *J. Comput. Phys.* **2016**, *307*, 321−332.
(48) Katzenmeier, L.; Carstensen, L.; Bandarenka, A. S. Li+ Conductivity of Space Charge Layers Formed at Electrified Interfaces Between a Model Solid-State Electrolyte and Blocking Au-Electrodes. *ACS Appl. Mater. Interfaces* **2022**, *14*, 15811−15817.
(49) Das, S.; Ghosh, A. Ionic Conductivity and Dielectric Permittivity of PEO-$LiClO_4$ Solid Polymer Electrolyte Plasticized with Propylene Carbonate. *AIP Adv.* **2015**, *5*, No. 027125.
(50) Yu, K.; Tian, Y.; Gu, R.; Jin, L.; Ma, R.; Sun, H.; Wei, X. Ionic Conduction, Colossal Permittivity and Dielectric Relaxation Behavior of Solid Electrolyte Li3xLa2/3-xTiO3 Ceramics. *J. Eur. Ceram. Soc.* **2018**, *38*, 4483−4487.

https://doi.org/10.1021/acs.jpcc.2c02481
J. Phys. Chem. C 2022, 126, 10900−10909